Research Article

Ha Vinh Ho, Eunsoo Choi*, and Jun Won Kang

Analytical bond behavior of cold drawn SMA crimped fibers considering embedded length and fiber wave depth

https://doi.org/10.1515/rams-2021-0066
received June 29, 2021; accepted August 17, 2021

Abstract: The NiTi SMA fibers were cold drawn to introduce prestrain, and then, they were made to crimped fibers with various wave depths. The recovery stress was measured, which was useful for closing the cracks in fiber-reinforced concrete. The pullout behaviors were also examined considering the existing recovery stress, and it is found that the recovery stress did not influence so much on the pullout behavior. According to the pullout results, a parametric study used a finite element analyzing (FEA) model to quantify the cohesive surface model's parameters and the value of the friction coefficient. Then, the developed model is used to investigate the crimped fiber's pullout behavior with various embedded lengths and wave depths. When the fiber in the elastic range, the peak stresses significantly raise due to increasing embedded waves; they show a linear relationship. After the yield of the SMA fiber, the peak stresses are also a function of embedded waves; however, the increasing trend is slow down. Concerning the cost, the even distribution of the fiber, and for guaranteeing the fiber experiences the pulling out, it is recommended that the embedded lengths and corresponding wave depths should be designed to avoid the yield.

Keywords: shape memory alloy, crimped fiber, unit pullout resistance, wave depth, embedded length

*** Corresponding author: Eunsoo Choi,** Department of Civil and Environmental Engineering, Hongik University, Seoul 04066, Republic of Korea, e-mail: eunsoochoi@hongik.ac.kr, tel: +82-2-320-3060, fax: +82-0-332-1244
Ha Vinh Ho: Department of Civil and Environmental Engineering, Hongik University, Seoul 04066, Republic of Korea, e-mail: hovinhha@mail.hongik.ac.kr
Jun Won Kang: Department of Civil and Environmental Engineering, Hongik University, Seoul 04066, Republic of Korea, e-mail: jwkang@hongik.ac.kr

1 Introduction

Various methods have been introduced to improve the characteristics of mortar or concrete, such as adding nanoparticles, polymeric materials, or fibers [1,2]. Adding fibers while producing a mortar or concrete mixture is an effective way to achieve this purpose at a low cost. Many studies have proved that added fibers can increase tensile ductility and the cementitious composite's impact resistance [3–6]. Due to the gradual pullout failure of embedded fibers, the concrete showed more pseudo-ductile behavior, increased residual strength, and enhanced energy dissipation [7,8]. The fibers' effect depends on their properties and the pullout resistance between the fibers and the cementitious matrix. Pullout resistance is essential to induce pullout force between the fiber and the mortar matrix to prevent slipping of the interface. A high pullout resistance ensures the composite behavior of fiber and mortar. According to the needed bond properties between fiber and matrix, various pullout experimental tests and mechanical analyses have been conducted to assess the fiber–matrix bond behavior.

Various surface treatments, such as acid etching, hand sanding, and sandblasting, have been studied; among these methods, sandblasting induces the highest resistance [9–11]. Creating an acid-etched surface is easier than other techniques; therefore, it is widely used to increase pullout resistance [12]. However, surface treatment is not economical because it is hard to improve surface conditions between the fibers and the cementitious matrix. A recent trend in increasing pullout resistance is to create fibers with discontinuous shapes. The pullout resistance includes adhesion and friction for straight fiber, determined by the surface condition between the fibers and the mortar matrix [13–15]. However, discontinuous fibers induce an anchoring bond due to their irregular shape in addition to adhesive and frictional resistance. Many researchers have used various fibers, such as polyvinyl alcohol, polypropylene, glass, and carbon fibers for

reinforcement [16]. However, only steel fiber and shape memory alloy (SMA) fiber can be used to create a discontinuous shape because of the reasonable deformability; the other fibers generally are used with a straight shape.

Previous studies have suggested various shapes, such as twisted, crimped, and hooked; all these shapes are available for the mass production of steel fiber. The crimped fibers provided the highest bond resistance among the aforementioned fibers; multiple crimped indentations function as multiple anchors that induce a strong anchoring bond. However, if crimped fibers are too weak, indentations will be stretched, and the pullout behavior is similar to that of straight fiber. The hooked shape is the second most effective one; the two hinges are too short compared to the total embedded length. The last one is the twisted shape, in which resistance is created by the untwisting torsional moment resistance [17,18]. For simulation, the straight, twisted, and hooked shapes are modeled and given out the same pullout behavior of experimental results; the pullout behavior is affected by various parameters such as fiber geometry, tensile strength, embedded length, and mortar strength [19–21].

Previous studies have validated some bond slip analytical models. Naaman et al. [22] conducted an experimental pullout test with smooth steel fiber of 25 mm length and with various cementitious matrix strengths to assess a prediction model. The model used the peak load, the corresponding end slip, and the initial portion of the curve slope to solve the characteristic bond stress versus the slip curve's critical parameters, namely, bond modulus, maximum shear stress, and maximum frictional shear stress. The predicted stress versus slip curve showed a good fit with the experimental curve at all matrix strengths. For hooked steel fiber, Alwan et al. [23] modeled the end hooks as two hinges, which were the cause of a chain of various parabolas, while Chanvillard [24] divided the fiber into distinct curves and straight parts. Laranjeira et al. [25] introduced a model, which was quite comparable with Alwan's model; however, the model did not consider fiber and matrix inclination. A semi-analytical model suggested by Soetens et al. [26] is applicable for straight fiber and a wide range of hooked types combined with various cementitious matrix strengths. For the finite element analysis, van der Aa [27] developed a model using ABAQUS software for straight and hooked steel fiber with a concrete matrix; three contact models were used to model the adhesive bond and frictional behavior.

SMA fiber has been used recently because of its unique properties, namely, the shape memory effect and the superelastic effect. The shape memory effect induces recovery stress as well as deformation recovery of SMA fibers when they are heated. The superelastic effect produces self-recovery stress when they are unloaded. Thus, these properties can provide crack closing [28,29], prestressing [30–32], crack repairing [33], and self-healing [34] of SMA fiber-reinforced cementitious composites. The recovery stress in the high prestrain level of the SMA fiber can delay the debonding, and the debonding stress increased with more prestrain [35,36]. Various SMA fiber shapes, such as L, N, dog bone, and paddle shaped, have been suggested [37]. Experimental tests have indicated that paddle-shaped fibers provide the highest bond resistance; the next most effective type is dog bone-shaped fibers. They are discontinuous at the end parts. Dog bone-shaped fibers can be mass produced by heating or by putting the end parts into boiled water, whereas the paddle-shaped fibers can be created only one by one. Recently, Choi et al. [38,39] reported that the crimped shape has the greater potential for SMA fibers. The pullout resistance of crimped fibers was 12 times and 10 times higher than that of straight and dog bone-shaped fibers, respectively. Moreover, fibers with this shape can be mass produced by the crimping of straight fibers.

The bond behavior of straight superelastic SMA fiber- and carbon fiber- reinforced polymers can be predicted by a 3D nonlinear finite-element method using ABAQUS software. Dawood et al. [40] conducted a pullout test with SMA fiber embedded between two layers of unidirectional carbon fiber fabric saturated by epoxy. The cohesive zone was used to model the interface, and the quantified parameters of the coherent model such as stiffness (K), maximum shear stress (τ_{max}), and damage energy (G) were indicated by comparison with the stress versus slip curves of the experimental test. El-Tahan and Dawood [41] improved Dawood's model with stress and strain parameters after debonding instead of the damage energy. The parameter of friction was not considered in those studies. It is found from the previous studies that there is a lack of the pullout model of crimped SMA fiber embedded in cementitious matrix to determine the exact values of pullout model's parameters.

The cold-drawn SMA fibers induce recovery stress and thus have the capacity of closing cracks in the fiber-reinforced concrete with heating; this phenomenon was called as crack closing. The crack-closing mechanism was depended not only on recovery stress but also on the bond resistance between the fibers and cementitious matrix. This study determined the recovery stress of straight and crimped SMA fibers and investigated the bond resistance of the fibers changed due to heating. Moreover, based on the test results, it is suggested a pullout model to further examine the effects of the embedded length and wave depth on the crimped fiber's pullout behavior. In particular, first,

the parameters of the cohesive surface model were investigated by considering the results obtained for straight fiber. Then, the friction coefficient was estimated by comparing the experimental and predicted outcomes of crimped fiber. Based on the observed model, crimped fiber's pullout behavior with various embedded lengths and wave depths is discussed.

2 Experimental test

2.1 Fabricate cold drawn SMA fibers

Ni50.4-Ti (wt%) SMA fibers were cold drawn to create the prestrain; then, a rolling device crimped them to produce crimped fibers. The starting austenite temperature (A_s) and finishing austenite temperature (A_f) of the fibers were 42.01 and 91.46°C, respectively. Those values were indicated by a thermo-analytical technique, namely, differential scanning calorimetry (DSC) [38]. The shape of the crimped fibers is shown in Figure 1, and Table 1 presents the dimensions of the straight (ST) and crimped (CR) fibers. The crimped fibers had four different wave depths of 0.055, 0.061, 0.091, and 0.124 mm. After crimping, the diameter of the crimped fibers did not change so much, which was estimated as less than 0.3%.

Table 1: Dimensions of straight and crimped fibers

Name	Diameter (mm)	Wave depth (mm)	Wavelength (mm)	Fiber length (mm)
ST	0.665	—	—	30
CR1	0.665	0.055	3.3	30
CR2	0.666	0.061	3.3	30
CR3	0.667	0.091	3.3	30
CR4	0.667	0.124	3.3	30

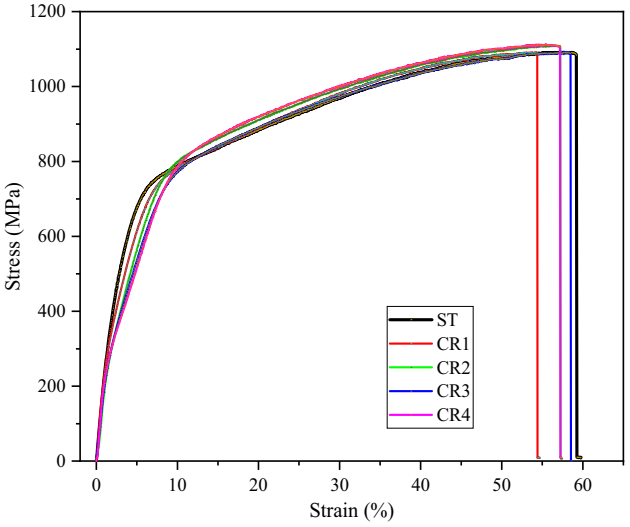

Figure 2: Monotonic tensile behavior of fibers.

2.2 Tensile behavior and recovery stress of cold drawn SMA fibers

Figure 2 shows the monotonic tensile behavior of cold-drawn fibers. All curves linearly increase up to 1.0% strain with the Young's modulus of 22.6 GPa. After that, the crimped fibers show softening behavior compared with straight fiber due to the stretching of indentation parts under tensile loading. The secant modulus of straight fiber is 10.5 GPa, while those of CR1 to CR4 fibers are 8.6, 7.5,

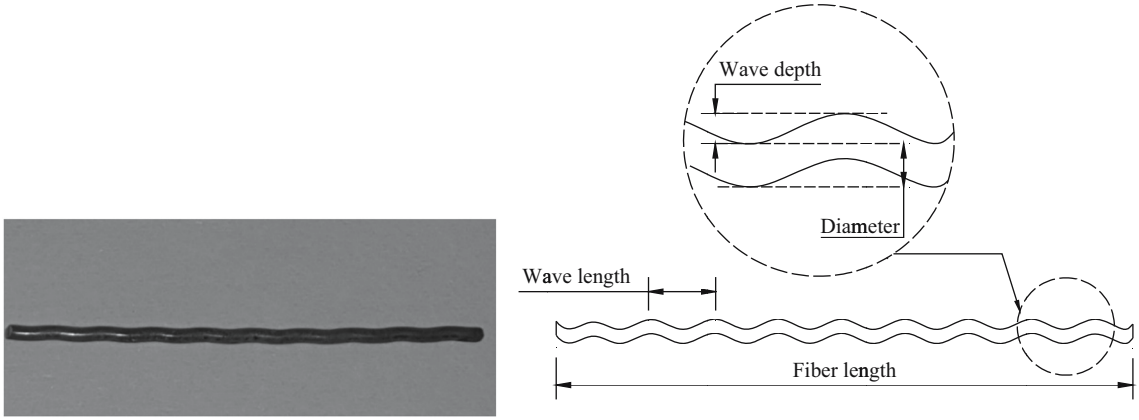

Figure 1: Photo of crimped fibers and illustration of dimensions.

7.0, and 6.9 GPa, respectively. The higher wave depth fiber is more stretched than a lower one; thus, crimped fiber's secant modulus decreases with the increasing wave depth. All fibers yield at the same stress of 730 MPa, and they rupture at 1,100 MPa with the ultimate strain of about 60%. Thus, the tensile behaviors of 0.665-mm diameter crimped fibers with wave depths ranging from 0.055 to 0.124 mm are not very different.

The cold-drawn SMA wire's tensile behavior depends on the area reduction ratio (ARR). When the ARR ranges from 7 to 10%, the phase transformation state looks disappeared and, then, the initial slope of the response became almost linear till the yield. Thus, the tensile behavior of straight cold drawn SMA wire in Figure 2 apparently showed elastoplastic behavior like steel material [42].

Choi et al. [39] indicated that the recovery stress increased when increasing the heating temperature up to a specific value; then, the stress decreased because the fiber was stretched along the fiber direction due to the thermal effect. The specific temperature produced maximal recovery stress was 230°C for fiber with 1.0 mm diameter and 160°C for 0.7 mm diameter. Therefore, in this study, the temperature of 150°C was chosen to heat the fiber. This temperature was higher than the finishing austenite temperature (91.46°C) to ensure the phase transformation happen, and it was lower than 160°C to reduce the thermal effect. The recovery stress–temperature curves of the ST and CR fibers presented in Figure 3a and b show maximal recovery stress as well as residual stress, which is the final recovery stress after heating the fiber from room temperature to 150°C and then cooled down to room temperature. In general, in the heating process, the recovery stress increased because all parts of the fibers gradually reached 150°C and completed phase transformation. The recovery stress decreases with decreasing the temperature because NiTi SMAs show such a trend. The maximal recovery stress and residual stress of the ST fiber were higher than those of the CR fibers. Moreover, more stress decreased with increasing the degree of crimping. For maximal recovery stress, the reductions were 21.8, 32.4, 37.4, and 44.1% for CR1 to CR4 fibers in comparison with ST fiber. The same trend occurred to residual stress.

2.3 Pullout behavior of cold drawn SMA fibers

2.3.1 Test setup

Figure 4 presents the dimensions of specimens and test setup. We put a half-length of a cold-drawn SMA fiber into a mortar specimen, which had a half dog bone shape. The compressive strength of the mortar specimen was 55 MPa, and the composition of the mortar is presented in Table 2. For each type of fiber, six specimens were fabricated. After 28 days, half of specimens was heated by an oven at 150°C in 6 h before conducting the pullout test, while the other half was not heated.

A grip system gripped the bottom part of the specimen, and the fiber was pulled by an actuator, which kept the fiber at 5 mm from the top surface of the specimen. On the top of the pullout system, a load cell measured the force applied, and the stroke of an actuator was set up to gauge the pullout displacement of fiber. The

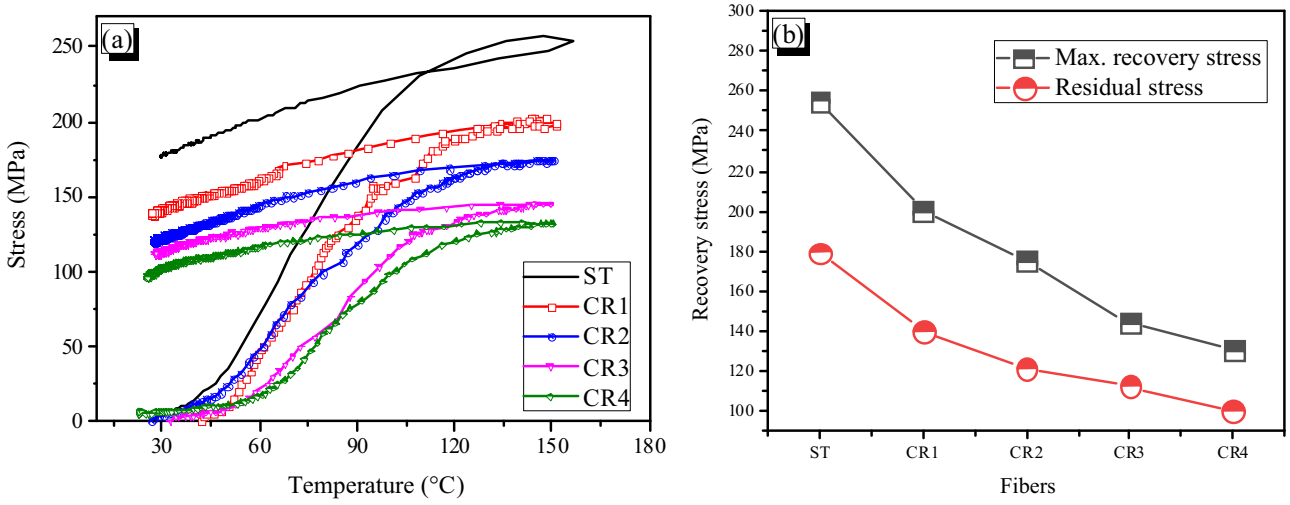

Figure 3: (a) Recovery stress curves at 150°C and (b) comparison maximal recovery stress and residual stress of ST and CR fibers.

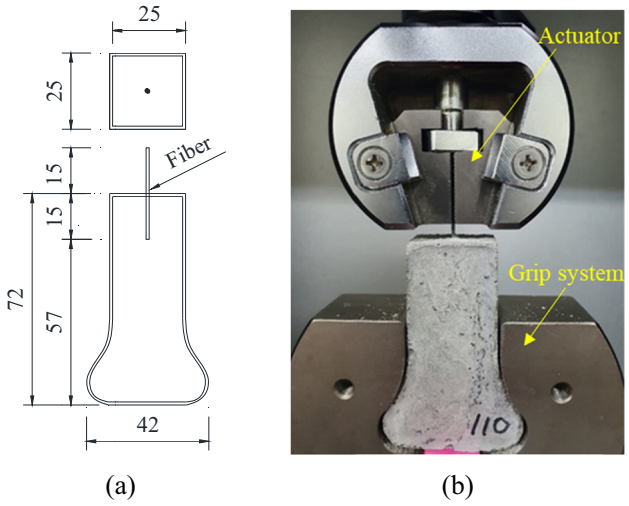

Figure 4: Test setup and dimensions of a specimen (unit: mm). (a) Dimensions of the specimen and (b) pullout test setup.

pullout speed was 1.0 mm·min^{-1}, and the response sampling rate was 5.0 Hz.

2.3.2 Experimental results

Figures 5 and 6 show the pullout stress versus displacement of the specimens and their averages. In the nonheating case, the ST fiber showed increasing bond stress until it reached a peak at 120 MPa due to adhesive resistance. Then, the fiber slipped because the adhesive resistance was broken. Frictional resistance contributed to the pullout stress in the next part; the frictional stress decreased with the increasing displacement. Because of a mistake in conducting the test, only two results of the ST fiber were obtained. However, the two pullout responses almost coincided; thus, they can represent the response of the ST fiber.

For crimped fiber, the pullout stress versus displacement curve reflects the shape of the fiber. Each wave's step is 3.3 mm, which is equal to the wavelength of the fiber; the pullout stresses reached the peak at the peak of indentations. The crimped fibers had 4½ waves embedded in the mortar matrix; however, the shape of curves is only evident in the first three waves. The stress at the last peak significantly decreases.

In comparison to the pullout behaviors of the CR fibers, the peak pullout stresses of the crimped fibers increased with increasing wave depth. The highest stress was about 730 MPa at the first peak of the CR4 fiber; this value equals the yield. Thus, the CR4 fiber with a 0.124-mm wave depth yielded, whereas the other crimped fibers with lower wave depths slipped and were deformed in the elastic part.

Even with the heating treatment, the pullout behavior of the CR SMA fibers did not change so much; the shapes of response curves in the two cases are almost the same. The comparison maximal pullout stress of the fibers for the nonheating and heating cases is presented in Figure 7. Except the CR2 fiber, the maximum pullout stresses of the heating cases are a little larger than those of the nonheated specimens. With heating, the fiber bulged in diameter and produced pressure to mortar duct; this led to the slightly increasing pullout resistance and, moreover, made the pullout response smooth.

In the concerning fiber shape, the CR fibers should be used for cementitious materials instead of the ST fiber because of the extremely higher pullout resistance. The CR fibers, moreover, provided the recovery stress for the composite, which cannot introduce by other types of fibers, such as steel, glass, and carbon fibers. Therefore, the CR fibers were suitable for crack closing. When the reinforced structures undergo loading and cracking, the fibers played as passive fibers, which bridged the cracks. The bond resistance and tensile behavior of the fibers mainly contributed to the bridging capacity. When applying the heating, the revery stress closed the crack width; in this phase, the bond resistance was critical for keeping the fiber not to be pulled out the matrix.

The pullout and tensile experimental results showed that the CR fibers with higher wave depth produced a relatively high bond resistance, while they provided smaller recovery stress. Therefore, the dimensions of crimped parts of CR fibers should be considered to guarantee providing a reasonable bond resistance as well as recovery stress. In the following sections, a pullout model is suggested for designing the CR fibers with considering the embedded length and the wave depth of the fibers. Because the tensile behavior of cold drawn SMA fiber was elastic–plastic as shown in Figure 2, this model can also be used for the other elastic–plastic fibers, such as steel fiber.

Table 2: Composition of the mortar

Portland cement (type III)	Fly ash	Silica sand	Water reducing admixture	Water
1.0	0.15	1.0	0.009	0.35

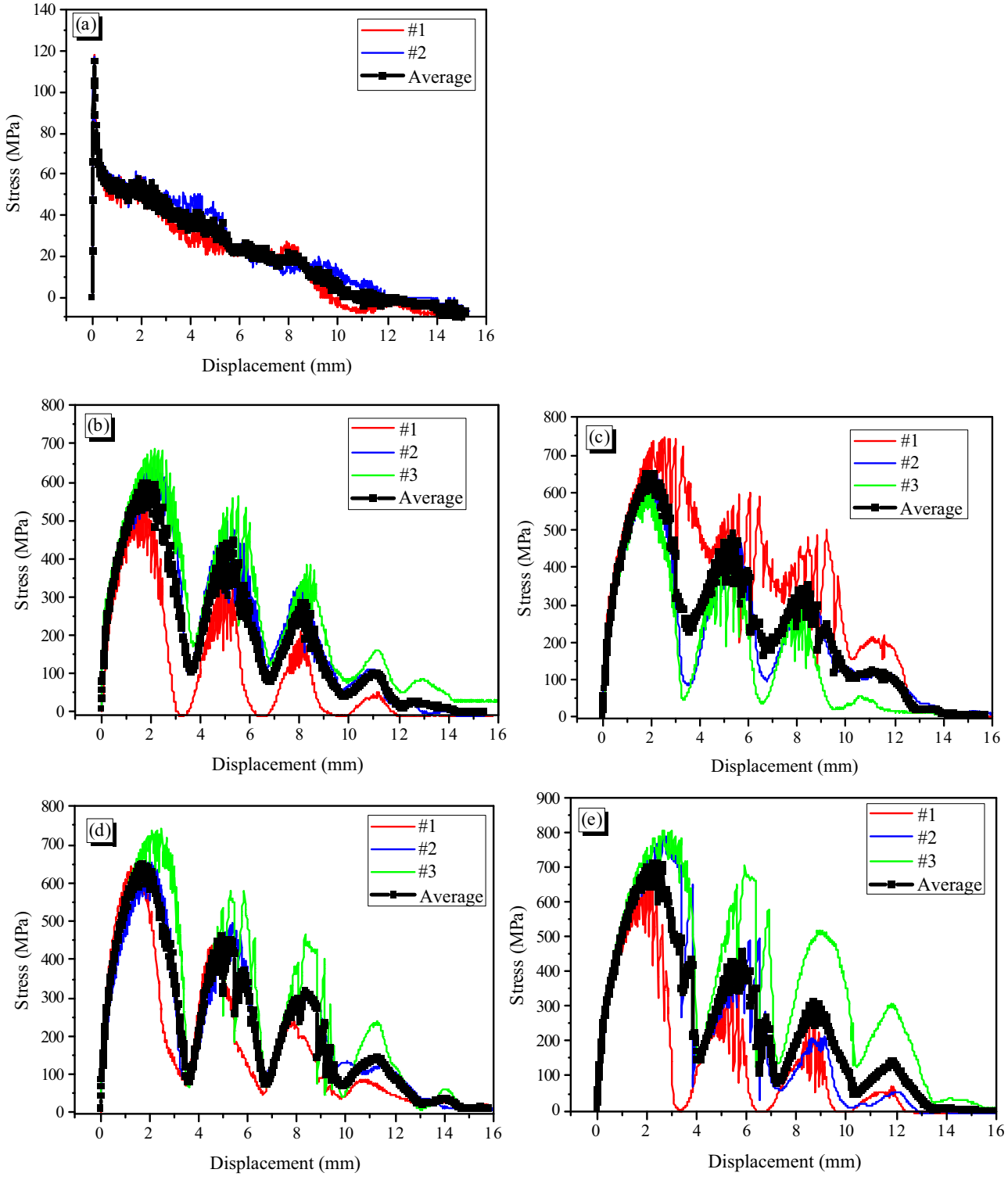

Figure 5: Pullout stress–displacement curves of the fibers in nonheating case: (a) ST, (b) CR1, (c) CR2, (d) CR3, and (e) CR4.

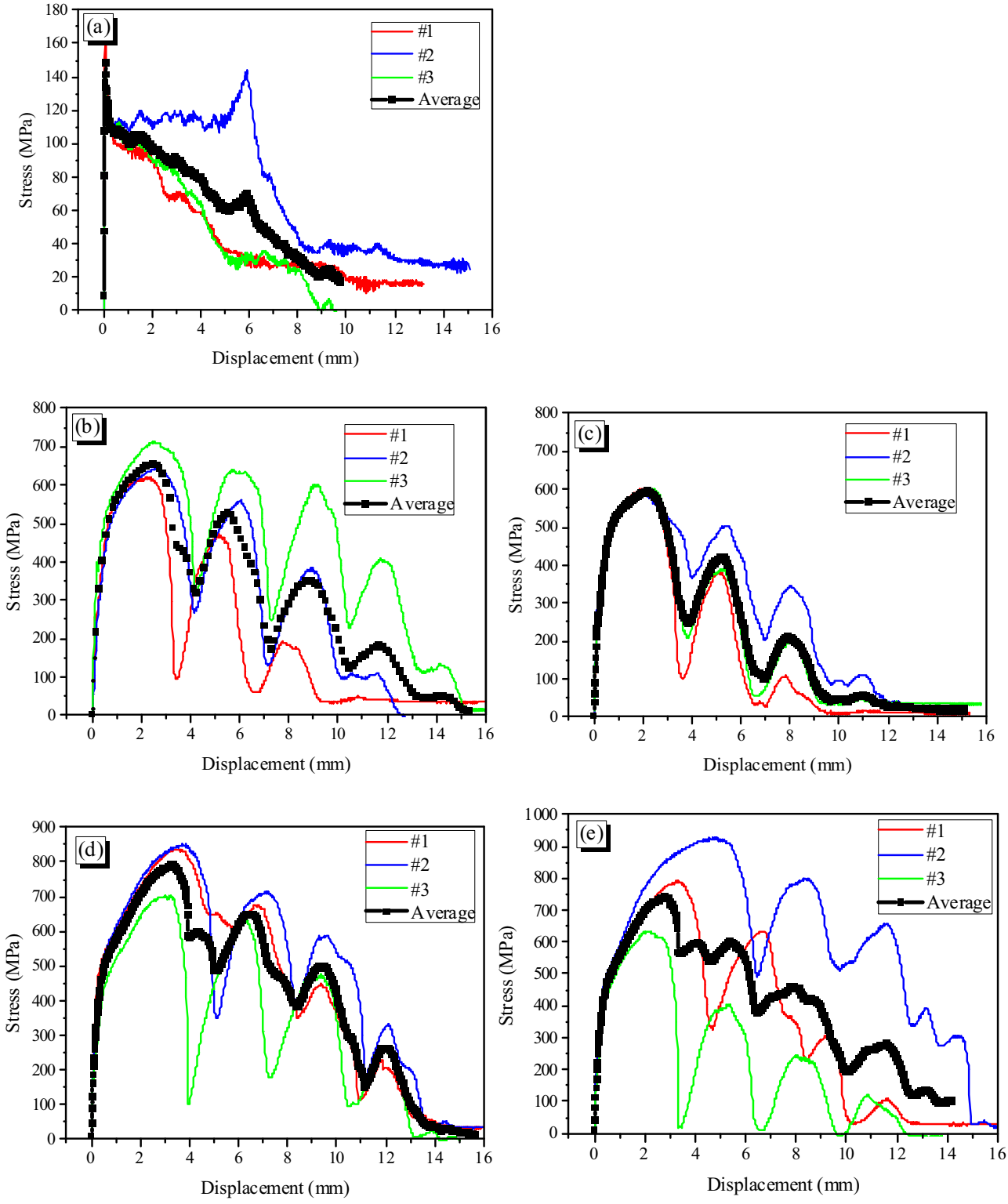

Figure 6: Pullout stress–displacement curves of the fibers in the heating case: (a) ST-H, (b) CR1-H, (c) CR2-H, (d) CR3-H, and (e) CR4-H.

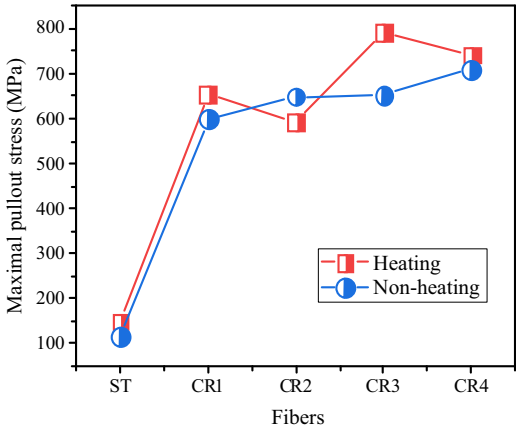

Figure 7: Comparison maximal pullout stress of the fibers with and without heating.

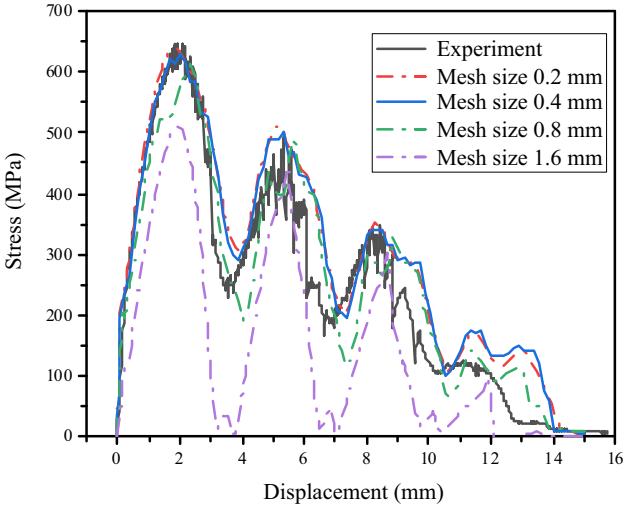

Figure 8: Convergence of stress response with respect to element sizes.

3 Numerical simulation

3.1 Finite-element model

A three-dimensional (3D) FEA was conducted using commercial software ABAQUS (version 3DEXPERIENCE R2019X, Dassault Systemes Simulia Corp.) to model the bond mechanism of cold drawn SMA fibers and mortar matrix. The finite-element model included two components: the mortar matrix and SMA fiber. The mortar matrix and the mono SMA fiber were defined as solid elements with eight-node continuum elements with three translational degrees of freedom at each node (element C8D3R). The fiber for models with the embedded length of 15 mm. The fiber and the duct in the mortar matrix were divided finely with 0.1 mm in perimeter and 0.4 mm in the longitudinal direction. With the mesh sizes of 0.8 and 1.6 mm in the longitudinal direction, the stress response of the FEA model differs from that of the experiment. However, when reducing the mesh size to 0.2 and 0.4 mm, the stress responses of the FEA model and experiment coincided (Figure 8). Thus, the mesh size of 0.4 mm is chosen to get the solution's convergence with the experimental results and reduce the computational time. The model used the auto-mesh feature; the total numbers of elements with the mortar matrix and SMA fiber were 3,000 and 1,760, respectively (Figure 9).

The displacement applied at the top surface of the SMA fiber was 15 mm with a 1 mm·min^{-1} pullout speed. We set the bottom surface of the mortar specimen as zero displacements in the pullout direction. The step size was set up automatically until convergence was achieved. The initial step size corresponded to a displacement of 0.1 mm, and between 40 and 200 time steps were completed.

The mortar matrix was modeled as an elastic material with the Poisson's ratio of 0.19. The value of E_c is indicated as $4{,}700\sqrt{f'_c}$ [43], where f'_c is the compressive strength. The damage properties and shrinkage effect of the mortar matrix were not considered in this study. Cold-drawn NiTi SMA fiber does not undergo phase transformation; thus, the elastic–plastic material built on the ABAQUS modeled the SMA fiber. The Poisson's ratio in the elastic part was 0.3. Figure 10 presents the typical tensile stress–strain curves of SMA fiber obtained from the finite-element model and the experimental test.

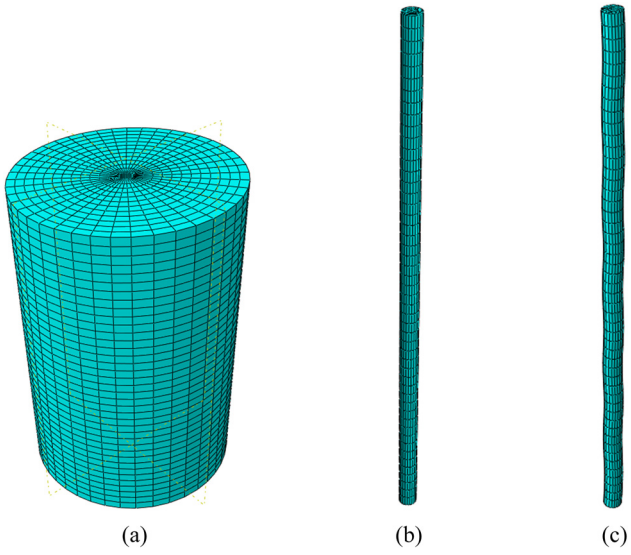

Figure 9: Dimensions of elements in the model and meshed model. (a) Fiber and matrix, (b) straight fiber, and (c) crimped fiber.

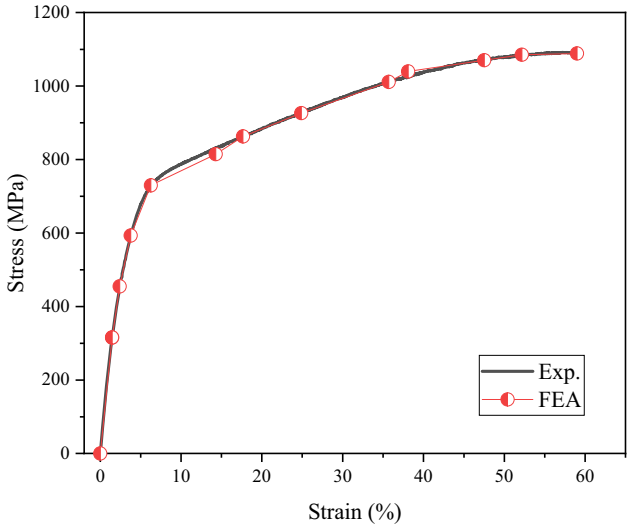

Figure 10: Modeling tensile behavior of SMA fiber.

3.2 Interaction properties

According to the previous studies, there are three load transfer mechanisms: adhesion, friction, and anchoring bond [44]. Straight fiber does not have an anchoring bond, which only exists in discontinuous fiber due to the interlocking of the discontinuous part of the fiber and the mortar matrix. Adhesive resistance develops before slipping occurs; then, the frictional resistance reduces due to the reduction of the embedded length. Adhesion is defined by the cohesive behavior of the contact surface, whereas the friction is dependent on the normal and tangent behaviors.

The master surface and the slave surface of surface-to-surface interaction are defined, in which the nodes of the slave surface do not penetrate the master surface. Based on the advice of ABAQUS [45], the larger surface should be defined as the master surface, while the smaller one should be defined as the slave surface. Thus, the mortar matrix's duct is defined as the master surface, while the surface of the SMA fiber is set as the slave surface.

3.2.1 Adhesive resistance

Traction separation behavior describes the adhesion behavior between an SMA fiber and a cementitious material or polymer composite [27,40]. The traction separation model assumes initially linear elastic behavior. The elastic behavior of traction stress and separation is expressed as follows:

$$t = \begin{Bmatrix} \sigma_n \\ t_1 \\ t_2 \end{Bmatrix} = \begin{bmatrix} K_{nn} & K_{n1} & K_{n2} \\ K_{n1} & K_{11} & K_{12} \\ K_{n2} & K_{12} & K_{22} \end{bmatrix} \begin{Bmatrix} \delta_n \\ \delta_1 \\ \delta_2 \end{Bmatrix} = K\delta, \quad (1)$$

where t is the nominal traction stress vector, which includes three components, namely, σ_n, which is a normal traction stress, and t_1 and t_2, which are shear stresses along the wire direction and in the tangential wire direction. Separation δ consists of three response separations, δ_n, δ_1, δ_2, and K is the stiffness matrix. The normal stiffness and tangential stiffness are noncoupled, as shown in Figure 11. The normal separation by itself does not increase the shear traction stress, and the shear separation by itself does not raise the cohesive stress in the normal direction; thus, K_{ij} $(i \neq j) = 0$. Equation (1) can be rewritten as follows [40]:

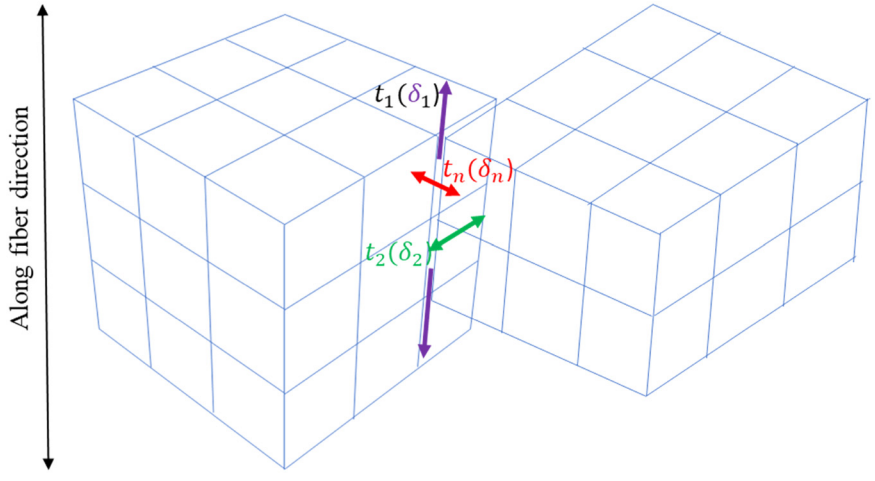

Figure 11: Traction separation behavior.

$$t = \begin{Bmatrix} \sigma_n \\ t_1 \\ t_2 \end{Bmatrix} = \begin{bmatrix} K_{nn} & 0 & 0 \\ 0 & K_{11} & 0 \\ 0 & 0 & K_{22} \end{bmatrix} \begin{Bmatrix} \delta_n \\ \delta_1 \\ \delta_2 \end{Bmatrix} = K\delta, \quad (2)$$

3.2.2 Debonding

Because the fiber is pulled out of the mortar matrix, the shear stress increases. When adhesion failure occurs, the interface between the matrix and the fiber does not fail at once; part of the stress still transfers through the interface. This process is called debonding, which finishes when the interface completely fails. The failure mechanism includes a damage initiation criterion and a damage evolution law. Damage initiation relates to the beginning of degradation of cohesive response; there are several damage initiation criteria, such as the maximum stress criterion, maximum separation criterion, quadratic stress criterion, and quadratic separation criterion. This study does not compare the accuracy of these criteria; thus, the popular quadratic stress criterion is used as a damage initiation criterion.

$$\left(\frac{\sigma_n}{\sigma_n^0}\right)^2 + \left(\frac{t_1}{t_1^0}\right)^2 + \left(\frac{t_2}{t_2^0}\right)^2 = 1, \quad (3)$$

where σ_n^0, t_1^0, and t_2^0 are the peak values of contact stresses when the separation is pure to the interface or the first/second shear direction. Because of the experimental test, σ_n and t_2 were negligible; only t_1 was eligible. The normal traction σ_n is put inside the Macaulay bracket to indicate that pure compression cannot lead to the initial damage. The damage evolution law is set as a linear degradation. Figure 12 shows the traction separation response for the cohesive surface.

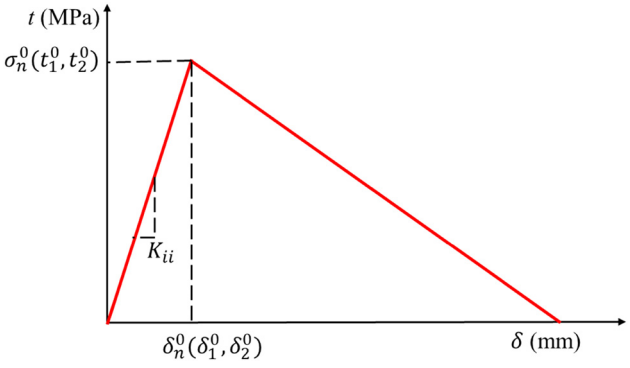

Figure 12: Cohesive surface model.

3.2.3 Combining debonding and friction

The interaction behavior after adhesion is the combination of debonding and friction. First, debonding is fully active, and friction is inactive. Then, debonding decreases, and friction increases due to slipping. As the damage increases, both debonding and friction partly contribute to the shear stress. Two linear and exponential softening models were built in ABAQUS to define the change from fully active debonding to completely active friction, as shown in Figure 13.

3.2.4 Friction resistance

When the fiber is no longer connected to the mortar matrix, there remains pullout stress until the fiber completely pulls out. This stress is caused by the friction between the fiber and the duct of the mortar. The friction behavior is set up in ABAQUS by normal behavior and tangent behavior.

Normal behavior is defined as "hard contact," which is set as the default in using contact pairs in ABAQUS [45]. The surfaces separate when the contact pressure between the surfaces is zero or negative, and the contact constraint is applied when the distance separating two surfaces becomes zero. For tangent behavior, the friction coefficient (μ) between two surfaces is used to define the friction. According to Coulomb's law of friction, shear stress is a function of the friction coefficient (μ) and normal stress (Figure 14). For a 3D model, the shear stress is defined in two directions with the assumption of a friction coefficient (μ). Because the normal force value is very small, the penalty method in ABAQUS is used for the calculation to get a high convergence rate.

4 Quantification of the parameters of the pullout model

4.1 Values of traction separation model parameters

According to Figure 4, the ST fiber shows a typical pullout stress versus displacement curve. The fiber shows increased bond stress until it reaches peak stress. The fiber' shape influences the pullout stress versus displacement curves; thus, the peak stress is not due to pure adhesion. Therefore,

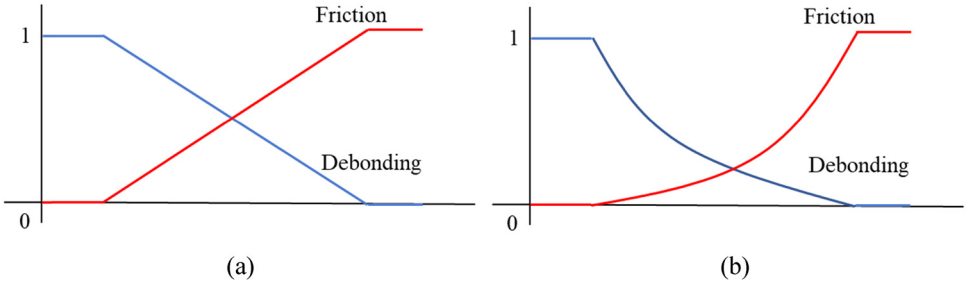

Figure 13: Combination of debonding and friction. (a) Linear softening model and (b) exponential softening model.

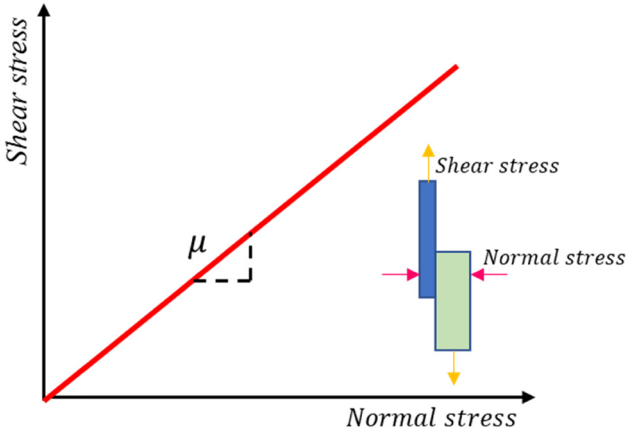

Figure 14: Coulomb's law of friction.

the cohesive surface model parameters were verified by comparison with the experimental test of ST fiber.

The two groups of finite-element models considered to quantify the parameters are summarized in Table 3. The value of δ_i^0, displacement at the finished bonding, is very small; this value was set as 0.5 mm based on the previous study [27]. Preliminary analyses select the values in this table to indicate the range of parameters. In group 1, the cohesive model is modeled as linear elastic without damage; the K parameter values range from 20 to 200 MPa·mm^{-1}. In group 2, t_i^0 ranges from 2 to 5 MPa, while the K value is fixed at 50 MPa·mm^{-1}.

In the adhesion part, the bond stress reaches a peak of 120 MPa at 0.1 mm; thus, the slope of increasing bond stress is 1,200. Figure 15 shows the pullout stress versus displacement curves of the finite-element analysis (FEA) models with various elastic stiffness values and the average curve of straight fiber in the experimental test.

A different error (DEK) is used to determine the best fit value of stiffness. The equation is calculated as follows:

$$\text{DEK} = |\text{Slop}_{\text{avg}} - \text{Slop}_{\text{FEA}}|, \tag{4}$$

where Slop_{avg} is the average slope obtained from the experimental test, and Slop_{FEA} is the slope predicted by FEA with various values of K. Figure 16 shows the effect of K on the DEK of the predicted model; the cohesive stiffness of 50 MPa·mm^{-1} minimizes the value of DEK. Thus, this value is chosen to fix the interfacial stiffness of the model.

In group 2, t_i^0 ranges from 2 to 5 MPa, whereas the K value is fixed at 50 MPa·mm^{-1} (Figure 17).

The different peak stress errors and corresponding displacement between experimental and FEA are named DES and DES-D, respectively. These values are calculated as follows:

Table 3: Ranges of values of cohesive surface model parameters

	K (MPa·mm^{-1})	t_i^0 (MPa)	δ_i^0 (mm)
Group 1	20, 30, 40, 50, 100, 200	—	—
Group 2	50	2, 2.5, 2.8, 3, 3.5, 5	0.5

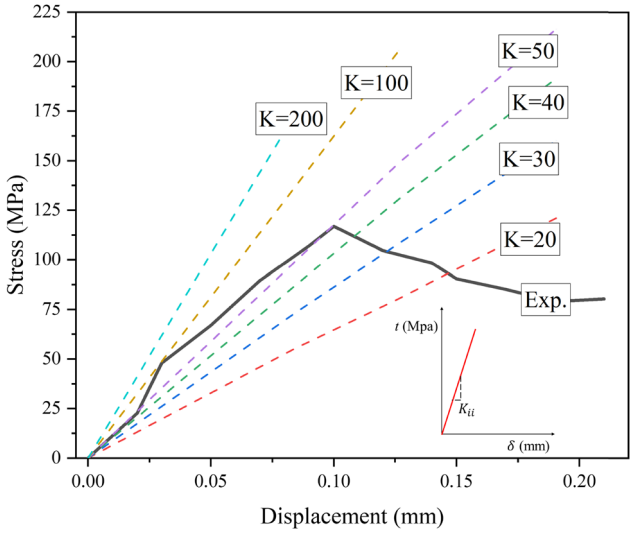

Figure 15: Determination of interfacial stiffness, K, according to the comparison of the experimental test and predicted model.

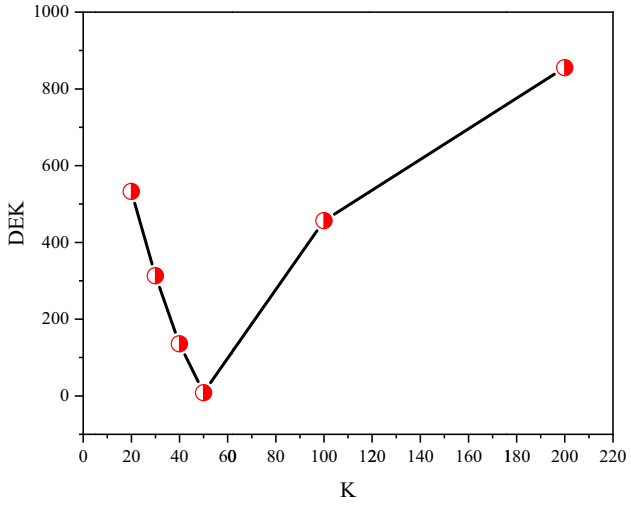

Figure 16: Relation of K in the predicted model and DEK value.

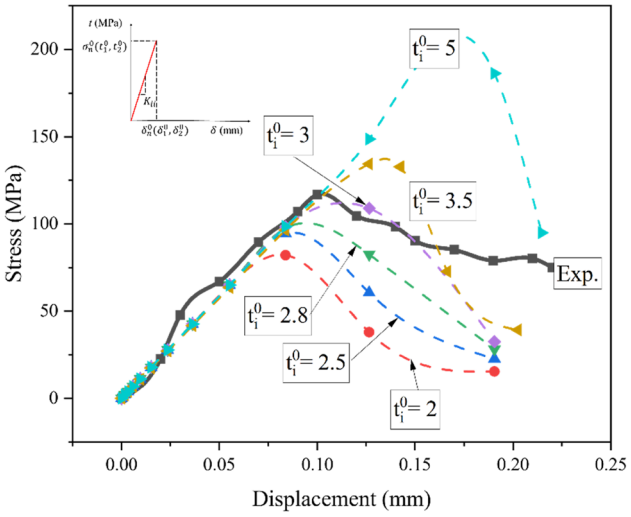

Figure 17: Determination of shear strength, t_i^0, according to the comparison of the experimental test and the predicted model.

$$\mathrm{DES} = |t_{\mathrm{avg}} - t_{\mathrm{FEA}}|, \tag{5}$$

$$\mathrm{DES\text{-}}D = |\delta_{\mathrm{avg}} - \delta_{\mathrm{FEA}}|, \tag{6}$$

where t_{avg}, δ_{avg}, t_{FEA}, δ_{FEA} are the average peak stress, the corresponding average strain in the experimental test, and those in the FEA model. Figure 18 shows the relation of DES, DES-D, and the t_i^0 parameter. When the value of shear strength, t_i^0, is less than 3.5 MPa, it does not affect the movement of the peak point much; however, with a higher shear strength, the DES-D significantly increases. The DES value is minimal when t_i^0 is 3 MPa.

Thus, the FEA model with straight SMA fiber indicates that $K = 50$ MPa·mm^{-1} and $t_i^0 = 3$ MPa are the optimal values of interfacial stiffness and shear strength, respectively.

4.2 Value of friction efficient

The exponential softening model for combining debonding and friction is used with the exponential parameter $\alpha = 6$ [27]. A friction coefficient (FR) of 0.3 or 0.33 has been used for most dry materials [46]. With the development of testing machines and testing methods, various friction coefficients for various contacting materials have been determined; the friction coefficient between steel and concrete or mortar can be up to 0.57 [47]. In this study, FRs ranging from 0.2 to 0.5 are used for the FEA models. The pullout stress of crimped fiber increases when the friction coefficient increases (Figure 19). The first three peaks of the curves made by the FEA model are a linear function similar to that in the experimental test. The fourth peak is significantly smaller than the other peaks.

A different error (DEF) is used to determine the best fit value of the friction coefficient. The equation is calculated as follows:

$$\mathrm{DEF} = |\sigma_{i\_\mathrm{peak\_exp}} - \sigma_{i\_\mathrm{peak\_FEA}}|, \tag{7}$$

where $\sigma_{i\_\mathrm{peak\_exp}}$, $\sigma_{i\_\mathrm{peak\_FEA}}$ are the first, second, and third peak stresses, ($i = 1 \div 3$), in the experiment and the FEA model. Figure 20 presents DEF values with various friction coefficients. When the FR is 0.3, the DEF has the smallest value; thus, the friction coefficient of the crimped fibers and mortar matrix is 0.3. This value does not change with the wave depth ranging from 0.055 to 0.124 mm. The friction coefficient is only dependent on the nature of the surface when the specimens are subjected to the same conditions. Thus, the friction coefficient is unchanged for all specimens with various wave depths. The friction force, however, increases with the increasing wave depth. The reason is that the friction force depends on the normal force exerted between surfaces; the increase in the wave depth of the mortar duct and crimped fiber leads to an increase in normal force.

5 The effect of the embedded length and wave depth of crimped fiber on pullout behavior

5.1 Free length

Free length is defined as the length of fiber from the upper mortar surface to the pullout actuator's pick point. For example, the free length in the experimental test

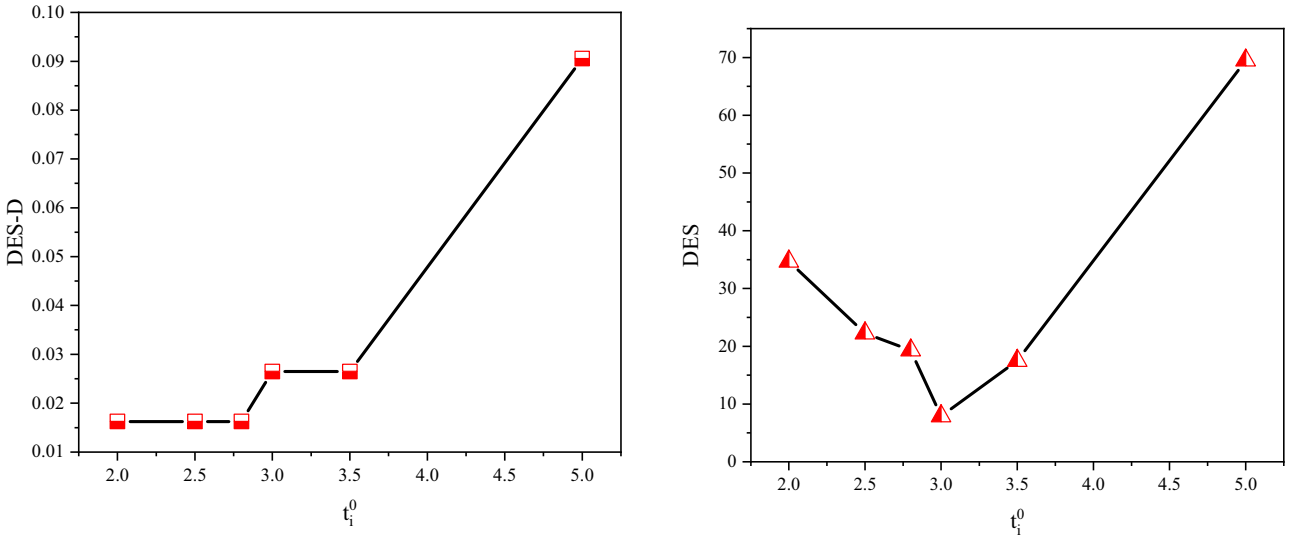

Figure 18: Relationship of DES versus t_i^0, and DES-D versus t_i^0.

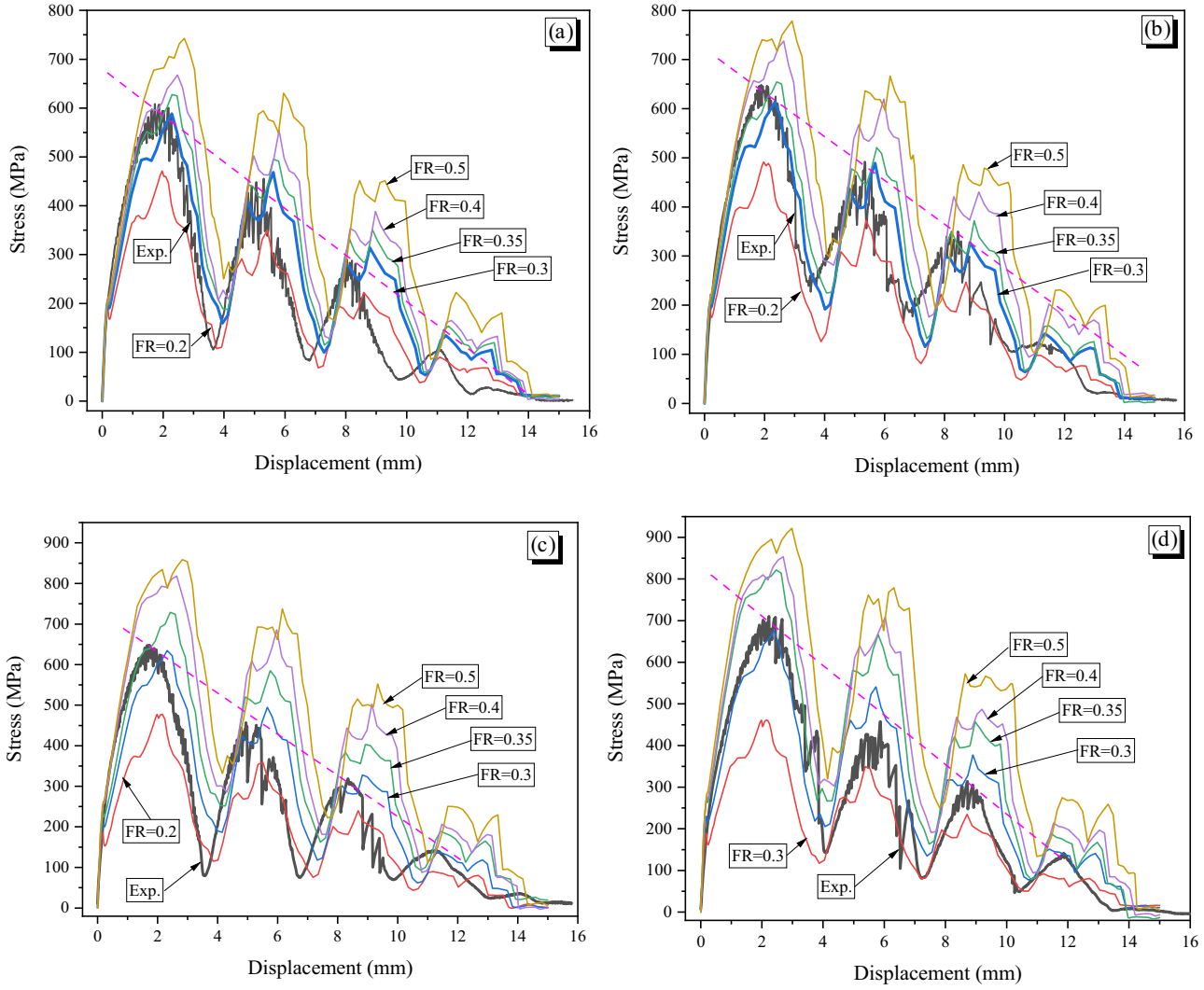

Figure 19: Pullout stress versus displacement curves of crimped fiber in FEA and experimental test: (a) CR1, (b) CR2, (c) CR3, and (d) CR4.

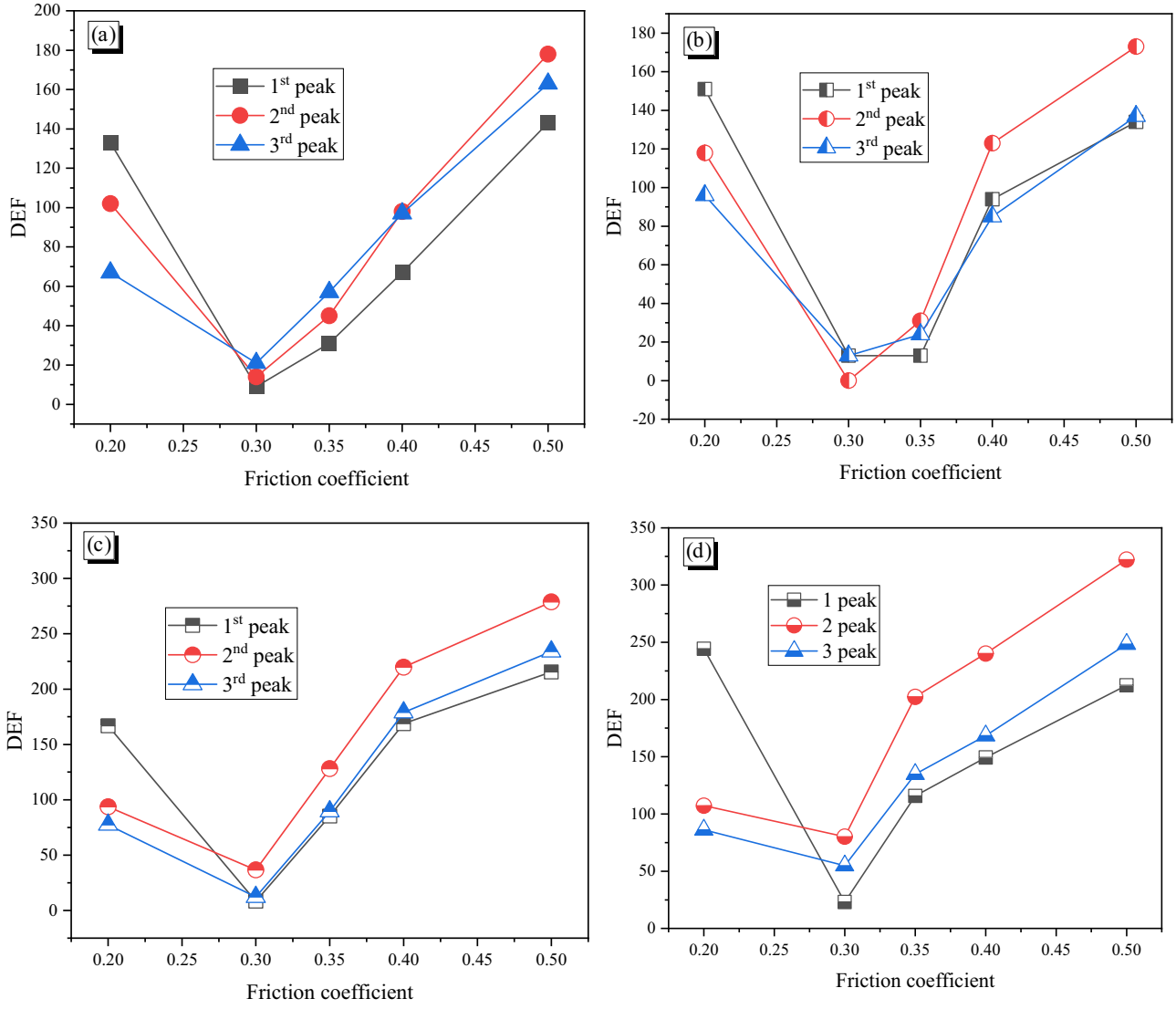

Figure 20: Relationship between DEF and friction coefficient: (a) wave depth = 0.055 mm, (b) wave depth = 0.061 mm, (c) wave depth = 0.091 mm, and wave depth = 0.124 mm.

(Section 2.3) is 5 mm. According to a previous paper, the free length can decrease the pullout stress of twisted steel fiber [19]; the effect of the free length is more noticeable for fiber with larger initial pitches. The free length can be minimized in an experiment but never eliminated. This section investigates the effect of the free length of fiber with various wave depths on crimped fiber's pullout stress curve. The curves of the experiment and the FEA model are shown in Figure 21.

In general, the peak stress is constant regardless of the free length. However, the curve is stretched a small distance from the beginning of the pullout process. The stretching develops until the first peak; then, the distance due to stretching becomes stable. The stretched distance can be explained by the physical stretching of the indentations of crimped fiber. The wave depth is shallow, that is, less than 0.124 mm; therefore, the distance is also tiny.

According to this result, the free length does not have much influence on crimped fiber's pullout behavior; however, future pullout experiments should minimize the free length to reduce the stretching distance. In the following sections, the model for investigating the embedded length and wave depth uses a free length of zero.

5.2 The effect of embedded length

In previous studies, aspect ratios (length/diameter) of embedded fibers ranging from 1/30 to 1/100 have been commonly used in experiments in which they were

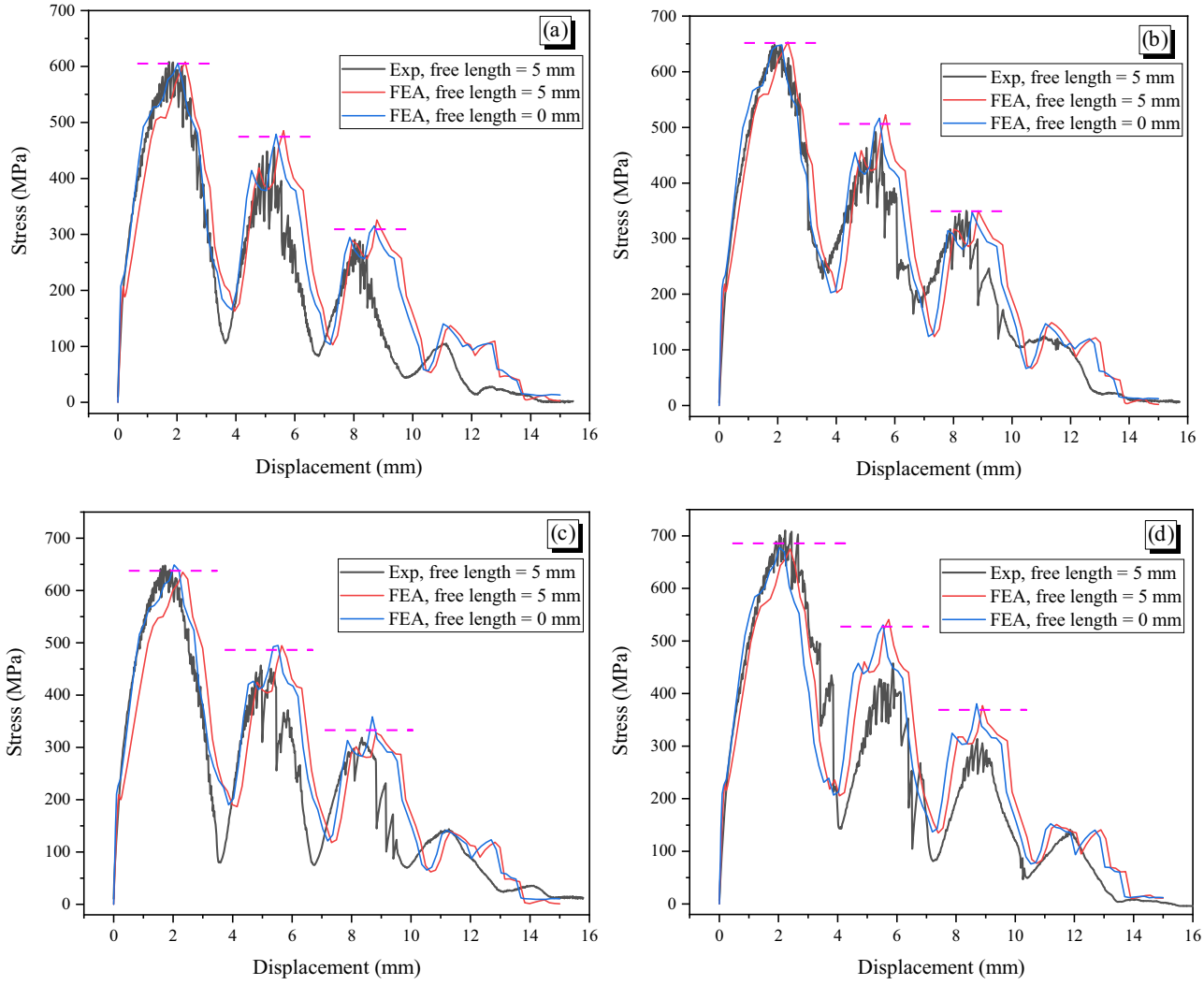

Figure 21: Influence of free length on the relationship between pullout stress and displacement: (a) wave depth = 0.055 mm, (b) wave depth = 0.061 mm, (c) wave depth = 0.091 mm, and wave depth = 0.124 mm.

embedded in cementitious materials [48]. In this study, the crimped fiber diameter was 0.665 mm; thus, the fiber length could range from 20 to 66.5 mm. Therefore, the pullout test's embedded length was modeled from 9.9 to 33 mm, which was three to ten times the wavelength.

With the embedded length of 15 mm (4½ waves) in the experimental test, the CR1 and CR2 fibers reached the maximal pullout stress of less than 650 MPa, while the crimped fibers with a relatively large wave depth induced a pullout stress nearly equal to the yield stress of 730 MPa. A crimped fiber with a large wave depth can yield or even rupture before it contributes fully to the postcracking strength. In this case, the fiber experienced like in a tensile test that is not a pullout test; this phenomenon was observed in a previous paper [49]. When the bond resistance is so strong, the fiber cannot be pulled out, and as a result, the curve of the pullout stress versus displacement is similar to that of tensile stress versus strain.

Conversely, the pullout resistance is a function of the embedded length [39]; thus, the stress increases with the increasing embedded length and does not reach the yield stress of the fiber. Thus, to guarantee that all fibers of various embedded lengths pull out, the wave depths of 0.055 and 0.061 mm were modeled. A schema illustrating the concept of the model is shown in Figure 22.

Figure 23 presents the pullout stress versus displacement curves of the crimped fibers. For numbers of embedded waves ranging from three to five, the pullout stresses at the peak points show a linear relationship. Those peak stresses are less than the tensile yield stress; thus, the crimped fibers with less than five embedded waves are pulled out with the

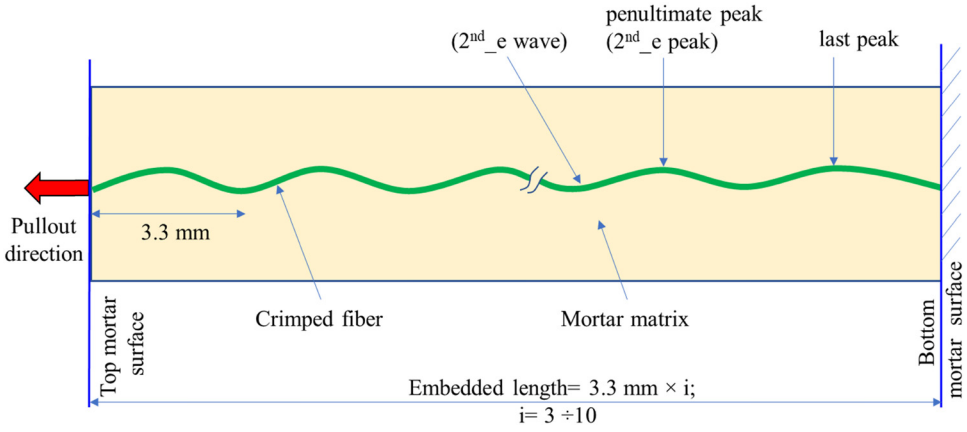

Figure 22: Schema of the pullout model.

elastic deformation. For longer embedded waves, the peak stresses of the added waves are higher than the yield stress of the crimped fiber. They also show a linear relationship. However, the slope is less than that of the line created by the stresses at the first five peaks. Thus, the relationship between the peak stresses of the crimped fiber is influenced by its tensile behavior. In the elastic part, the pullout stress at the peak significantly increases with additional embedded waves. However, the increasing trend becomes blunt when the crimped fiber is in the hardening region after yielding.

The slope of the line connecting the peak stresses decreases with the increasing embedded length. This means that the reduction of peak stress after each wave of the long embedded fiber is smaller than that of the short one. Thus, the long embedded fiber can maintain a relatively high pullout resistance with a large slip. However, long embedded fibers increase the cost of a composite material, and it can be the cause of flocculation and heterogeneous distribution [50].

Figure 24 shows the relationship between peak stress and embedded length, in which the last peak stress of each curve is ignored because it is very small. The peak stress increases with the embedded length; however, the increasing trend becomes dull with a long embedded fiber. The stresses at the penultimate (2nd_e), antepenultimate (3rd_e), and pre-antepenultimate (4th_e) peaks are approximately 300, 500, and 600 MPa, respectively. Thus, the difference between the penultimate peak and the antepenultimate peak is 200 MPa, while that between the antepenultimate peak and the preantepenultimate peak is only 100 MPa. The difference in stress between two adjacent peak points is called the unit pullout resistance per wave of the crimped fiber. The maximum peak stress of the 10-wave fiber is 867 MPa, which is 20.4% higher than the maximum peak stress of the five-wave fiber of 720 MPa. Thus, the length of the 10-wave fiber increased is double that of the five-wave fiber, whereas the increment of pullout resistance is not proportional to the length. This indicates that increasing the length of the crimped fiber is not effective if its maximum peak stress exceeds the fiber's yield stress.

Figure 25a presents the relationship between the unit pullout resistance of a wave and the order of the embedded wave. The effect of a wave of crimped fiber on pullout resistance is reduced with the increasing embedded length. For the last four peaks, the unit pullout resistance of a wave significantly decreases linearly, as shown in Figure 25b. After the fourth peak, the unit pullout resistance becomes stable at approximately 30–50 MPa.

The peak stresses of the fibers with a 0.061-mm wave depth are higher than those with 0.055-mm wave depth (see Figure 24). The average increase in peak stresses is 25 MPa (3.5%), with an increase of 0.006 mm in the wave depth. Moreover, making crimped fiber with various wave depths is easy by adjusting the gap between the rolling device's two crimper gears [38,39]. Thus, changing the wave depth of crimped fiber with the embedded length of about five waves is an effective and low-cost way to achieve enough pullout resistance. In contrast, the fiber is not ruptured during the pullout process.

5.3 The effect of wave depth

Crimped fiber with an embedded length of 16.5 mm (5 waves) was modeled with various wave depths ranging from 0.015 to 0.075 mm. Figure 26a shows the pullout stress curves as a function of displacement of the crimped

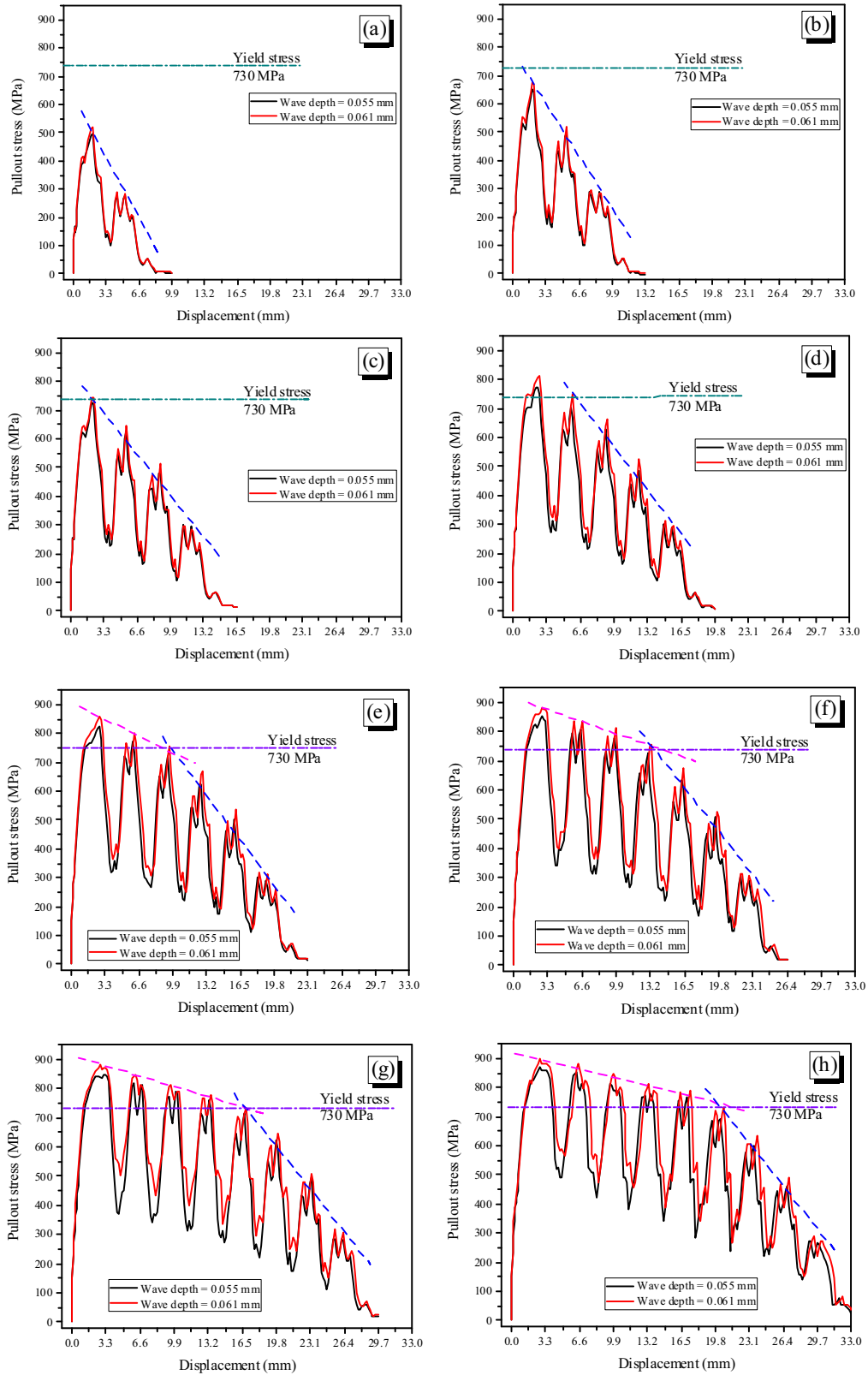

Figure 23: Pullout stress versus slip curves with numbers of waves ranging from 3 to 10: (a) 3 waves, (b) 4 waves, (c) 5 waves, (d) 6 waves, (e) 7 waves, (f) 8 waves, (g) 9 waves, and (h) 10 waves.

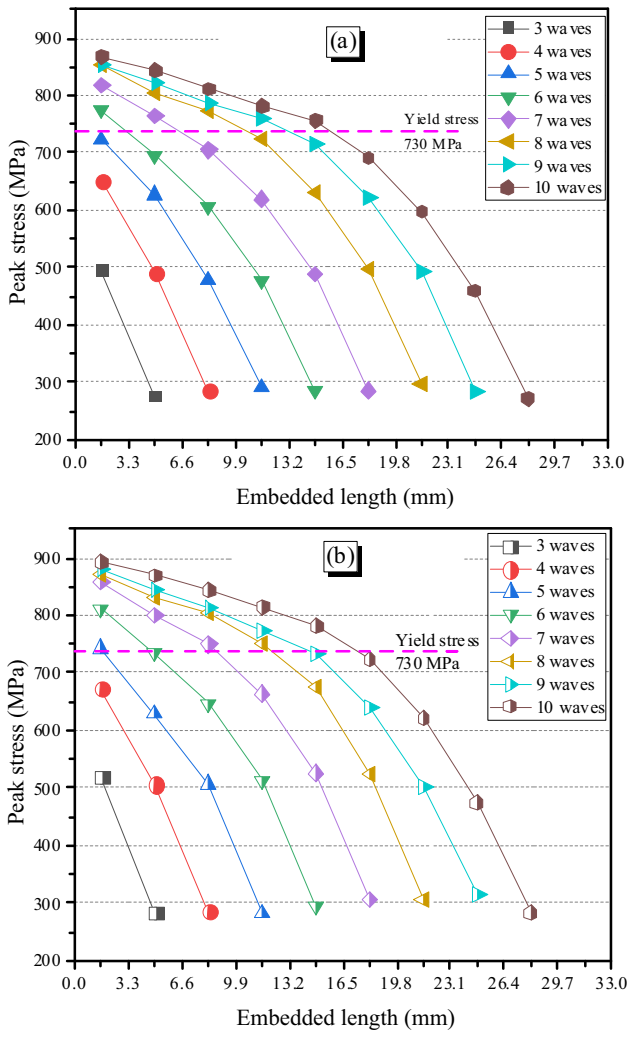

Figure 24: Pullout stress at the peak points with various numbers of embedded waves: (a) Wave_depth = 0.055 mm and (b) Wave_depth = 0.061 mm.

fibers, and Figure 26b presents the peak stresses. In general, the peak stresses increase with the increasing wave depth. The first peak of crimped fiber with a 0.075 mm wave depth is about 800 MPa, which exceeds the yield stress of the crimped fiber. Thus, it is unnecessary to consider wave depths greater than 0.075 mm.

For the wave depth of 0.015 mm, the maximal peak pullout stress is 340 MPa, which is 2.5 times higher than the 15-mm embedded ST fiber's peak stress in the experimental test. Moreover, after the peak, the ST fiber shows significantly reduced pullout stress without any peak stress, while the crimped fiber shows the relatively high pullout stresses at the peaks. Indentation of a crimped SMA fiber even with a low wave depth improves the pullout behavior between the SMA fiber and mortar matrix. In Figure 27a, the slopes of lines connecting the peaks of the pullout curves increase with the increasing wave depth. This indicates that the fiber with a lower wave depth is stretched less than the fiber with a higher wave depth. The peak stress at each peak point can be predicted by the linear function of wave depth (see Figure 27b).

These observations suggest that the pullout resistance of a crimped fiber with a small embedded length can increase with the increasing wave depth. For example, the 9.9 mm fiber having three waves with a 0.105 mm wave depth shows yielding, and another fiber with a 0.905-mm wave depth reaches the yield stress with a length of 13.2 mm having four waves. Therefore, a crimped SMA fiber can be designed to induce its yield stress, which is considered as the most effective fiber.

A crimped fiber in the elastic region shows a linear relationship between the peak stress and wave depth. The slopes of the linear relationship increase with an

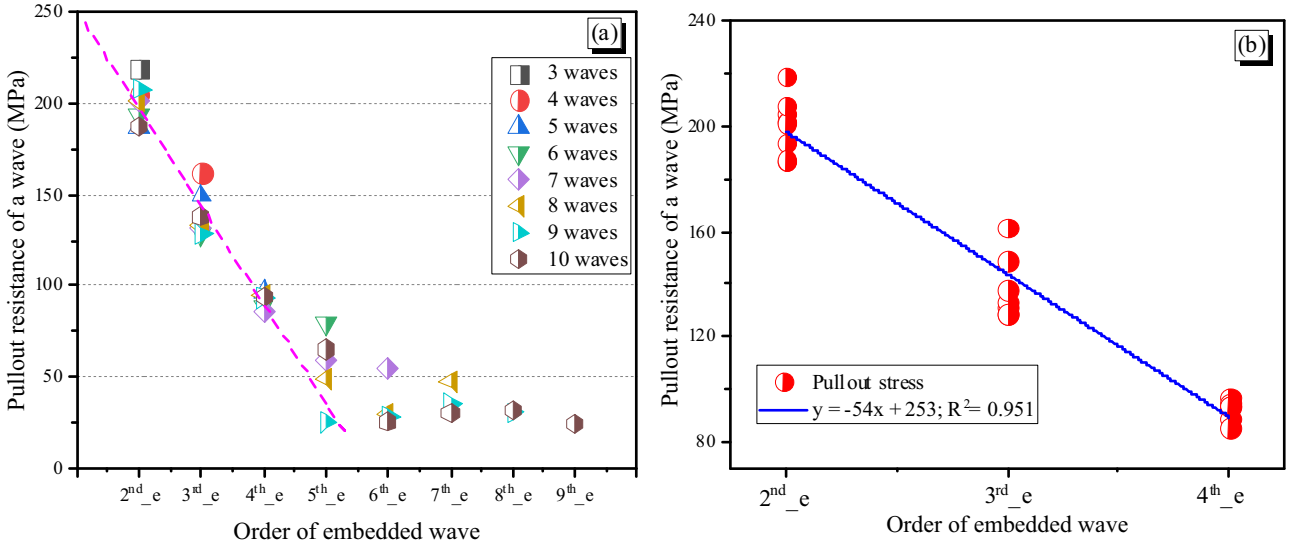

Figure 25: Pullout stress of each wave with various numbers of embedded waves. (a) Value of unit pullout resistance per wave, (b) Linear relationship between the unit pullout resistance per wave and the last four peaks.

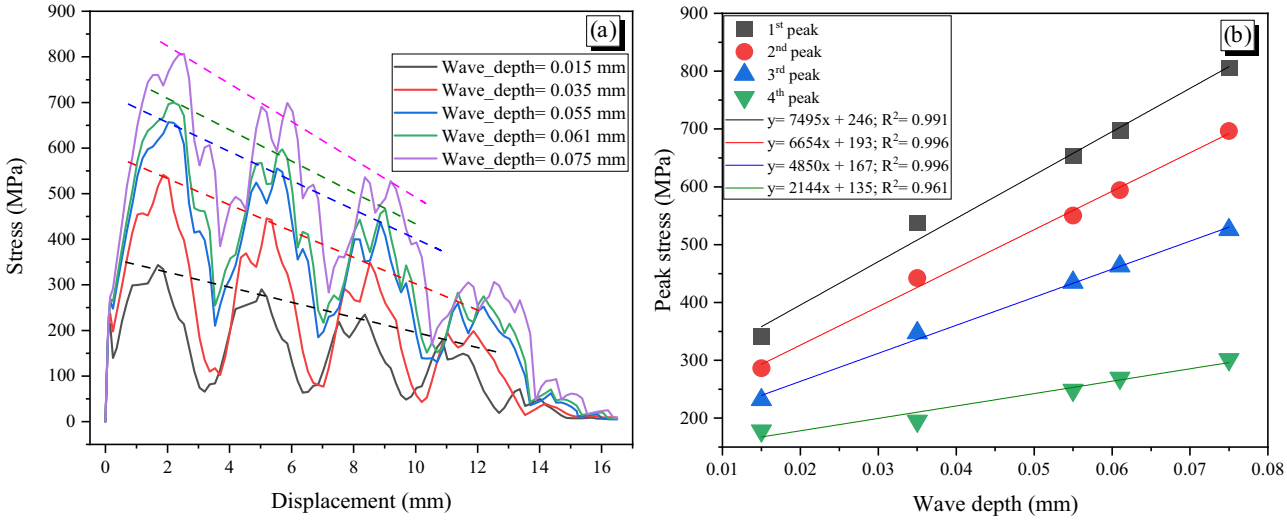

Figure 26: Relationship between pullout stress and wave depth of five-wave crimped fiber: (a) pullout curves and (b) peak stress versus wave depth.

increasing number of embedded waves. For example, the slope of the first peaks of the five-wave fiber is 7,495, which is larger than the corresponding values of the three- and four-wave fibers of 6,064 and 5,513, respectively (see Figure 27). Therefore, these findings indicate that the effect of wave depth on pullout stress for the short embedded length is weaker than that for the long embedded length.

6 Conclusion

Cold-drawn straight and crimped fibers with the same diameter of 0.665 mm were embedded in the mortar matrix at the same level of 15 mm. The fibers were pulled out monotonically until failure. Based on the experimental test, a parametric study was carried out using the FEA model to quantify the cohesive surface model's parameters and friction coefficient at the interface between the SMA fiber and the mortar matrix. Once the parameters were identified, the same values of parameters were used to investigate the effect of embedded length and wave depth on crimped fiber's pullout resistance. Based on the results of the experiments and the FEA model, the following conclusions can be drawn:

- The cohesive surface model is defined by the parameters of interfacial stiffness, K, and the interfacial shear strength, t_i^0. The values of K and t_i^0 were found

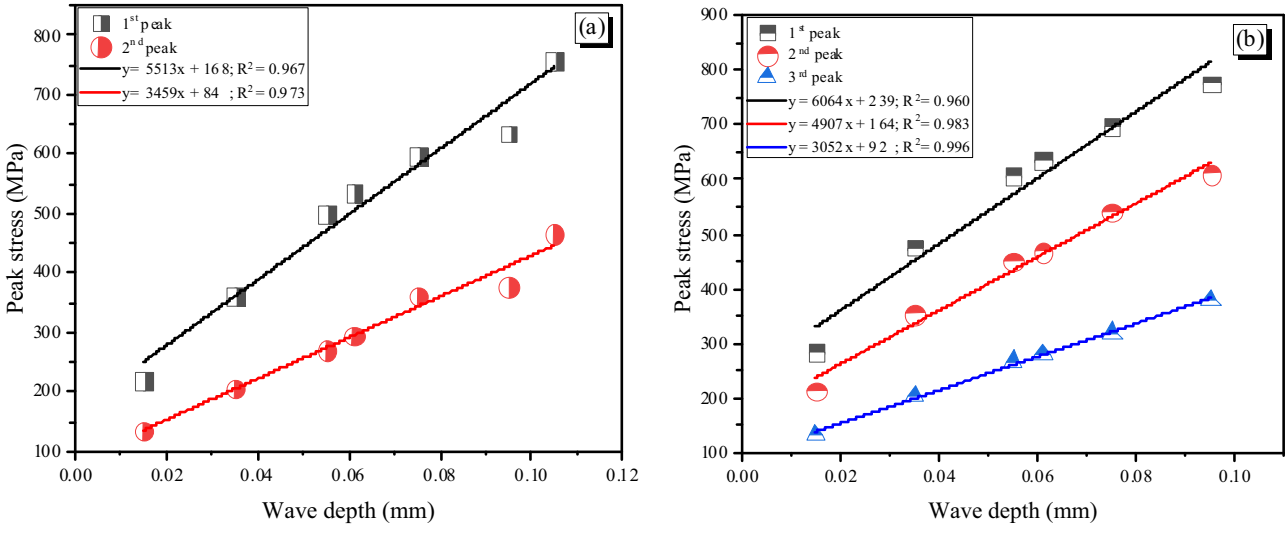

Figure 27: Relationship between pullout stress and wave depth of three- and four-wave fibers: (a) 3 waves and (b) 4 waves.

to be 50 MPa·mm^{-1} and 3 MPa, respectively, for the tested specimens. When damage cohesion occurs, the combination of debonding and friction is used with the exponential parameter $\alpha = 6$. The friction coefficient was identified as 0.3 for crimped fiber, regardless of the wave depth, ranging from 0.055 to 0.124 mm.

- The pullout stress significantly increases with the increasing embedded length if the fiber remains in the elastic range. Thus, the peak stresses of a crimped fiber before yielding can be predicted by a linear regression as a function of the number of waves. Beyond the yielding of the fiber, the unit pullout resistance of the crimped fibers is equal to approximately 30 MPa. Thus, for a crimped fiber with a 0.665-mm diameter and 0.061-mm wave depth, its embedded length is recommended to be five times the wavelength. Moreover, for more than five embedded waves, the crimped fiber yields and may not induce full pullout resistance capacity.
- A crimped fiber even with very small indentations can increase the pullout resistance significantly in comparison with a straight fiber. Therefore, crimped fiber is more applicable than other shapes because the overall shape of a crimped fiber with small indentations is similar to that of a straight fiber.
- The analytical result obtained in this work for crimped SMA fiber can be used to design a crimped SMA fiber to avoid yielding considering the fiber's diameter, wave depth and length, as well as mortar strength.

Acknowledgement: The authors acknowledge financial supports from the Basic Science Research Program through the National Research Foundation of Korea (NRF) funded by the Ministry of Education, Science and Technology (Project No. NRF 2020R1A4A-1018826).

Funding information: This research was supported by the Basic Science Research Program through the National Research Foundation of Korea (NRF) funded by the Ministry of Education, Science and Technology (Project No. NRF 2020R1A4A-1018826).

Authors contribution: Conceptualization, E.C., H.V.H.; methodology, E.C., H.V.H. and J.W.K.; formal analysis, H.V.H. and J.W.K.; investigation, E.C., H.V.H. and J.W.K; resources, E.C.; data curation, E.C. and J.W.K.; writing – original draft preparation, H.V.H.; writing – review and editing, E.C. and J.S.; visualization, H.V.H.; supervision, E.C.; project administration, E.C.; and funding acquisition, E.C. All authors have read and agreed to the published version of the manuscript.

Conflicts of interest: The authors declare no conflict of interest.

References

[1] Han, J., D. Wang, and P. Zhang. Effect of nano and micro conductive materials on conductive properties of carbon fiber reinforced concrete. *Nanotechnology Reviews*, Vol. 9, No. 1, 2020, pp. 445–454.

[2] Lapčík, L., M. Vašina, B. Lapčíková, M. Staněk, M. Ovsík, and Y. Murtaja. Study of the material engineering properties of high-density poly (ethylene)/perlite nanocomposite materials. *Nanotechnology Reviews*, Vol. 9, No. 1, 2020, pp. 1491–1499.

[3] Gao, D., L. Zhao, and G. Chen. Flexural behavior of fiber and nanoparticle reinforced concrete at high temperatures. *Fire and Materials*, Vol. 42, No. 7, 2018, pp. 725–740.

[4] Vahidi Pashaki, P., M. Pouya, and V. A. Maleki. High-speed cryogenic machining of the carbon nanotube reinforced nanocomposites: Finite element analysis and simulation. *Proceedings of the Institution of Mechanical Engineers, Part C: Journal of Mechanical Engineering Science*, Vol. 232, No. 11, 2018, pp. 1927–1936.

[5] Yuan, G., Y. Bai, Z. Jia, D. Hui, and K. T. Lau. Enhancement of interfacial bonding strength of SMA smart composites by using mechanical indented method. *Composites Part B: Engineering*, Vol. 106, 2016, pp. 99–106.

[6] Hu, H., P. Papastergiou, H. Angelakopoulos, M. Guadagnini, and K. Pilakoutas. Mechanical properties of SFRC using blended manufactured and recycled tyre steel fibres. *Construction and Building Materials*, Vol. 163, 2018, pp. 376–389.

[7] Rahmani, T., B. Kiani, M. Shekarchi, and A. Safari. Statistical and experimental analysis on the behavior of fiber reinforced concretes subjected to drop weight test. *Construction and Building Materials*, Vol. 37, 2012, pp. 360–369.

[8] Nili, M. and V. Afroughsabet. Combined effect of silica fume and steel fibers on the impact resistance and mechanical properties of concrete. *International Journal of Impact Engineering*, Vol. 37, No. 8, 2010, pp. 879–886.

[9] Jonnalagadda, K., G. E. Kline, and N. R. Sottos. Local displacements and load transfer in shape memory alloy composites. *Experimental Mechanics*, Vol. 37, No. 1, 1997, pp. 78–86.

[10] Payandeh, Y., F. Meraghni, E. Patoor, and A. Eberhardt. Debonding initiation in a NiTi shape memory wire–epoxy matrix composite. Influence of martensitic transformation. *Materials & Design*, Vol. 31, No. 3, 2010, pp. 1077–1084.

[11] Poon, C. K., L. M. Zhou, W. Jin, and S. Q. Shi. Interfacial debond of shape memory alloy composites. *Smart Materials and Structures*, Vol. 14, No. 4, 2005, id. N29.

[12] Cai, S., C. Wu, W. Yang, W. Liang, H. Yu, and L. Liu. Recent advance in surface modification for regulating cell adhesion and behaviors. *Nanotechnology Reviews*, Vol. 9, No. 1, 2020, pp. 971–989.

[13] Jang, B. K. and T. Kishi. Adhesive strength between TiNi fibers embedded in CFRP composites. *Materials Letters*, Vol. 59, No. 11, 2005, pp. 1338–1341.

[14] Gebuhr, G., M. Pise, M. Sarhil, S. Anders, D. Brands, and J. Schröder. Analysis and evaluation of the pull-out behavior of hooked steel fibers embedded in high and ultra-high-performance concrete for calibration of numerical models. *Structural Concrete*, Vol. 20, No. 4, 2019, pp. 1254–1264.
[15] Maleki, V. A. and N. Mohammadi. Buckling analysis of cracked functionally graded material column with piezoelectric patches. *Smart Materials and Structures*, Vol. 26, No. 3, 2017, id. 035031.
[16] Liu, J., N. Farzadnia, and C. Shi. Effects of superabsorbent polymer on interfacial transition zone and mechanical properties of ultra-high-performance concrete. *Construction and Building Materials*, Vol. 231, 2020, id. 117142.
[17] Guo, Z., Q. Zhu, W. Wu, and Y. Chen. Research on bond–slip performance between pultruded glass fiber-reinforced polymer tube and nano-CaCO3 concrete. *Nanotechnology Reviews*, Vol. 9, No. 1, 2020, pp. 637–649.
[18] Jung, C. Y. and J. H. Lee. Crack closure and flexural tensile capacity with SMA fibers randomly embedded on tensile side of mortar beams. *Nanotechnology Reviews*, Vol. 9, No. 1, 2020, pp. 354–366.
[19] Alhijazi, M., Q. Zeeshan, Z. Qin, B. Safaei, and M. Asmael. Finite element analysis of natural fibers composites: A review. *Nanotechnology Reviews*, Vol. 9, No. 1, 2020, pp. 853–875.
[20] Lei, M., Z. Chen, H. Lu, and K. Yu. Recent progress in shape memory polymer composites: methods, properties, applications and prospects. *Nanotechnology Reviews*, Vol. 8, No. 1, 2019, pp. 327–351.
[21] Maage, M. Interaction between steel fibers and cement-based matrixes. *Matériaux et Construction*, Vol. 10, No. 5, 1977, pp. 297–301.
[22] Naaman, A. E., G. G. Namur, J. M. Alwan, and H. S. Najm. Fiber pullout and bond slip. II: Experimental validation. *Journal of Structural Engineering*, Vol. 117, No. 9, 1991, pp. 2791–2800.
[23] Alwan, J. M., A. E. Naaman, and P. Guerrero. Effect of mechanical clamping on the pull-out response of hooked steel fibers embedded in cementitious matrices. *Concrete Science and Engineering*, Vol. 1, No. 1, 1999, pp. 15–25.
[24] Chanvillard, G. Modeling the pullout of wire-drawn steel fibers. *Cement and Concrete Research*, Vol. 29, No. 7, 1999, pp. 1027–1037.
[25] Laranjeira, F., C. Molins, and A. Aguado. Predicting the pullout response of inclined hooked steel fibers. *Cement and concrete research*, Vol. 40, No. 10, 2010, pp. 1471–1487.
[26] Soetens, T., A. Van Gysel, S. Matthys, and L. Taerwe. A semi-analytical model to predict the pull-out behaviour of inclined hooked-end steel fibres. *Construction and Building Materials*, Vol. 43, 2013, pp. 253–265.
[27] van der Aa, P. J. Biaxial stresses in steel fibre reinforced concrete modelling the pull out-behaviour of a single steel fibre using FEM. *Faculty of architecture building and planning unit structural desing concretete structures*, Einhoven University of Technology, Eindhoven, The Netherlands, 2014.
[28] Yoo, D. Y. and S. Kim. Comparative pullout behavior of half-hooked and commercial steel fibers embedded in UHPC under static and impact loads. *Cement and Concrete Composites*, Vol. 97, 2019, pp. 89–106.
[29] Ellis, B. D., D. L. McDowell, and M. Zhou. Simulation of single fiber pullout response with account of fiber morphology. *Cement and Concrete Composites*, Vol. 48, 2014, pp. 42–52.
[30] Cunha, V. M., J. A. Barros, and J. M. Sena-Cruz. Pullout behavior of steel fibers in self-compacting concrete. *Journal of Materials in Civil Engineering*, Vol. 22, No. 1, 2010, pp. 1–9.
[31] Abdallah, S. and D. W. Rees. Comparisons between pull-out behaviour of various hooked-end fibres in normal–high strength concretes. *International Journal of Concrete Structures and Materials*, Vol. 13, No. 1, 2019, id. 27.
[32] Choi, E., D. J. Kim, Y. S. Chung, H. S. Kim, and C. Jung. Crack-closing of cement mortar beams using NiTi cold-drawn SMA short fibers. *Smart Materials and Structures*, Vol. 24, No. 1, 2014, id. 015018.
[33] Lee, K. J., J. H. Lee, C. Y. Jung, and E. Choi. Crack-closing performance of NiTi and NiTiNb fibers in cement mortar beams using shape memory effects. *Composite Structures*, Vol. 202, 2018, pp. 710–718.
[34] Moser, K., A. Bergamini, R. Christen, and C. Czaderski. Feasibility of concrete prestressed by shape memory alloy short fibers. *Materials and Structures*, Vol. 38, No. 5, 2005, pp. 593–600.
[35] Choi, E., H. K. Hong, H. S. Kim, and Y. S. Chung. Hysteretic behavior of NiTi and NiTiNb SMA wires under recovery or prestressing stress. *Journal of Alloys and Compounds*, Vol. 577, 2013, pp. S444–S447.
[36] Rojob, H. and R. El-Hacha. Self-prestressing using iron-based shape memory alloy for flexural strengthening of reinforced concrete beams. *ACI Structural Journal*, Vol. 114, No. 2, 2017, id. 523.
[37] Choi, E., D. J. Kim, H. Youn, and T. H. Nam. Repairing cracks developed in mortar beams reinforced by cold-drawn NiTi or NiTiNb SMA fibers. *Smart Materials and Structures*, Vol. 24, No. 12, 2015, id. 125010.
[38] Choi, E., H. S. Kim, and T. H. Nam. Effect of crimped SMA fiber geometry on recovery stress and pullout resistance. *Composite Structures*, 2020, id. 112466.
[39] Choi, E., H. V. Ho, and J. S. Jeon. Active reinforcing fiber of cementitious materials using crimped NiTi SMA fiber for crack-bridging and pullout resistance. *Materials*, Vol. 13, No. 17, 2020, id. 3845.
[40] Dawood, M., M. W. El-Tahan, and B. Zheng. Bond behavior of superelastic shape memory alloys to carbon fiber reinforced polymer composites. *Composites Part B: Engineering*, Vol. 77, 2015, pp. 238–247.
[41] El-Tahan, M. and M. Dawood. Bond behavior of NiTiNb SMA wires embedded in CFRP composites. *Polymer Composites*, Vol. 39, No. 10, 2018, pp. 3780–3791.
[42] Choi, E., B. Mohammadzadeh, D. Kim, and J. S. Jeon. A new experimental investigation into the effects of reinforcing mortar beams with superelastic SMA fibers on controlling and closing cracks. *Composites Part B: Engineering*, Vol. 137, 2018, pp. 140–152.
[43] Choi, E., D. Kim, J. H. Lee, and G. S. Ryu. Monotonic and hysteretic pullout behavior of superelastic SMA fibers with different anchorages. *Composites Part B: Engineering*, Vol. 108, 2017, pp. 232–242.
[44] American Concrete Institute. *Building Code Requirements for Structural Concrete (ACI 318-14) and Commentary*, American Concrete Institute, Farmington Hills, MI, USA, 2014.
[45] Abrams, D. A. *Tests of bond between concrete and steel*, University of Illinois at Urbana Champaign, College of Engineering, Engineering Experiment Station, Champaign, USA, 1913.

[46] Hibbett, Karlsson, Sorensen. *ABAQUS/standard: User's Manual*, Vol. 1, Hibbitt, Karlsson & Sorensen, Rhode Island, USA, 1998.
[47] Blau, P. J. The significance and use of the friction coefficient. *Tribology International*, Vol. 34, No. 9, 2001, pp. 585–591.
[48] Rabbat, B. G. and H. G. Russell. Friction coefficient of steel on concrete or grout. *Journal of Structural Engineering*, Vol. 111, No. 3, 1985, pp. 505–515.
[49] Yazıcı, Ş., G. İnan, and V. Tabak. Effect of aspect ratio and volume fraction of steel fiber on the mechanical properties of SFRC. *Construction and Building Materials*, Vol. 21, No. 6, 2007, pp. 1250–1253.
[50] Choi, E., A. Ostadrahimi, and J. H. Lee. Pullout resistance of crimped reinforcing fibers using cold-drawn NiTi SMA wires. *Construction and Building Materials*, Vol. 265, 2020, id. 120858.